JOURNAL OF APPLIED CRYSTALLOGRAPHY

ISSN 1600-5767

Received 5 January 2015
Accepted 7 May 2015

Edited by G. Kostorz, ETH Zurich, Switzerland

Keywords: Zn–Cu alloys; grain refinement; heterogeneous nucleation; edge-to-edge matching.

Crystallography of grain refinement in cast zinc–copper alloys

Zhilin Liu,[a] Dong Qiu,[a] Feng Wang,[a,b] John A. Taylor[a] and Mingxing Zhang[a]*

[a]School of Mechanical and Mining Engineering, The University of Queensland, Brisbane, QLD 4072, Australia, and [b]BCAST, Brunel University, Uxbridge, Middlesex UB8 3PH, UK. *Correspondence e-mail: mingxing.zhang@uq.edu.au

Adding the peritectic forming element Cu effectively reduced the average grain size of cast Zn by over 85%. At a specified cast condition, the smallest grain size was obtained at 2 wt% Cu addition. A further increase in Cu content led to grain coarsening in the cast Zn–Cu alloys. Although the solute effect of Cu was predominately responsible for the grain refinement through restriction of the grain growth, it was found that the variation of grain size is also closely related to the formation of the pro-peritectic phase, ε-$CuZn_4$. Crystallographic calculations using the edge-to-edge matching model showed low interatomic misfit and interplanar mismatch between Zn and the ε-$CuZn_4$ phase. In addition, a reproducible h.c.p.–h.c.p. (h.c.p. denotes hexagonal close-packed) orientation relationship between Zn and the ε-$CuZn_4$ particles (located within the Zn grain centres) was also experimentally determined using the electron backscattered diffraction method. This indicated the high potency of the pro-peritectic ε-$CuZn_4$ particles as effective heterogeneous nucleation sites for η-Zn, which further refined the Zn grains. However, when the Cu content was over 2.0 wt%, formation of large ε-$CuZn_4$ particles resulted in grain coarsening of the cast alloys.

1. Introduction

The purpose of grain refinement in cast metals is to produce uniformly distributed equiaxed (or near equiaxed) grains in order to eliminate the anisotropic properties of a columnar structure (Greer *et al.*, 2003; StJohn *et al.*, 2011) and to improve both the ductility and strength of the materials. Furthermore, a well refined microstructure is also associated with enhanced casting soundness, reduced chemical segregation and porosity, decreased hot tearing potency, and, more importantly, improved formability in the subsequent forming process (Mohanty & Gruzleski, 1995; Murty *et al.*, 2002; McCartney, 1989) for castings or ingots. Generally, grain refinement can be achieved through dynamic nucleation (Stefanescu, 2002) and inoculation (Greer *et al.*, 2003). The former is associated with forced localized convection, such as stirring and fast cooling to produce secondary nuclei or to increase the nucleation rate. The latter is the most widely used approach in industry, aiming to promote heterogeneous nucleation and to limit grain growth through addition of effective grain refiners into the liquid metal before casting. During the inoculation process, the inoculant particles and the solutes can be simultaneously added *via* master alloys. The inoculant particles act as heterogeneous nucleation sites. The solutes provide restriction to grain growth. For instance, the Al–5Ti–B master is used to refine Al alloys, in which both inoculant particles (Al_3Ti and/or TiB_2) and solute (Ti) are added together (Greer *et al.*, 2000). Another typical example is the addition of a Zr-containing master alloy to refine the Al/

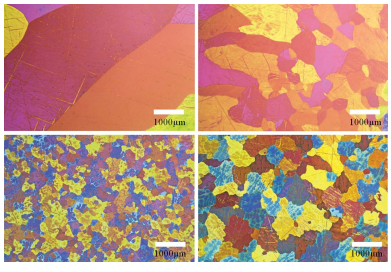

Mn/Si-free Mg alloys (Emley, 1966; Qian & Das (2006). The Zr particles are the inoculants and the Zr solute provides restrictions to grain growth. Generally, the inoculants are either formed *in situ* or externally introduced into the melt (Greer *et al.*, 2000; Johnsson *et al.*, 1993; Zhang, Kelly, Qian & Taylor, 2005; Qiu & Zhang, 2009; Bramfitt, 1970). Al_3Ti and Zr particles can be introduced either through *in situ* formation, because both Al–Ti and Mg–Zr are peritectic systems, or through external addition. But, TiB_2 can only be externally added. Al_2Y, which is another effective nucleant particle in the Y-containing Mg alloys, has been *in situ* formed through adding Al (Qiu, Zhang, Taylor & Kelly, 2009). Other reported inoculants for Mg alloys, such as ZnO (Fu *et al.*, 2008), AlN (Fu *et al.*, 2009) and SiC (Easton *et al.*, 2006), were externally added. The questions that arise are (*a*) which type of compounds can be used as effective inoculants and (*b*) how to identify such compounds for a particular base alloy.

Because the most effective grain refiners, such as Al_3Ti for Al alloys, Zr for Mg alloys (Easton & StJohn, 1999*a*; Wang, Liu *et al.*, 2013; Exner & Petzow, 1985; Izumi *et al.*, 1993; Glardon & Kurz, 1981; Barker & Hellawell, 1974) and Sb for Sn alloys (Chen *et al.*, 2008), are related to peritectic reactions, Banerji *et al.* (1989) proposed a peritectic solidification approach. It was considered that the primary grains of an alloy are formed on the pro-peritectic particle *via* the peritectic reaction (Crosley & Mondolfo, 1951). Subsequently, this theory has been introduced to elucidate the mechanism of grain refinement in peritectic based alloys (Emley, 1966; Crosley & Mondolfo, 1951; Wang, Qiu *et al.*, 2013; Wang *et al.*, 2014; Qiu, Zhang & Kelly, 2009; McDonald & Sridhar, 2003; Davies *et al.*, 1970). However, it has long been debatable whether the peritectic reaction directly contributes to grain refinement. First, when Ti, Zr and Ag were added to refine the cast Al, Mg and Zn alloys, significant grain refining efficiency could be achieved, even with solute additions that were far below the maximum solubilities of Ti, Zr and Ag in Al, Mg and Zn alloys, respectively. According to the Al–Ti, Mg–Zr and Zn–Ag binary phase diagrams, peritectic reaction does not occur when the solute content is below its maximum solubility (Qian & Das, 2006; Lee *et al.*, 2000; Easton & StJohn, 1999*b*; Liu *et al.*, 2013). Moreover, it was also argued that peritectic reactions cannot occur in the practical solidification process, because peritectic reactions rely on the solute diffusion in a solid. In a 'real' solidification process, the solute diffusion is too slow to promote the peritectic reaction (Qian & Das, 2006; StJohn, 1990; StJohn & Qian, 2009).

Heterogeneous nucleation and the solute paradigm are two widely accepted theories to understand the mechanism of grain refinement. Most new grain refiners for cast metals were developed on the basis of these theories (Qiu, Zhang, Taylor & Kelly, 2009; Wang, Qiu *et al.*, 2013; Wang *et al.*, 2014; Qian *et al.*, 2009; Fan *et al.*, 2009). It is considered that effective heterogeneous nucleation particles possess a low interfacial energy with the metal matrix, which controls the grain refining potency (Bramfitt, 1970). Higher grain refining efficiency can be achieved if the interfacial energy between the particles and the primary solid is low. Generally, the interfacial energy is associated with interfacial structure, atomic matching, interface orientation and/or the chemical environment (Bramfitt, 1970; Qiu & Zhang, 2013). Therefore, it is almost impossible to accurately and quantitatively describe the interfacial energy. A simple approach to evaluate the grain refining potency of a crystalline particle is based on crystallographic calculation of the atomic mismatch (CAM) across the particle/matrix interface, because better atomic matching (lower mismatch) corresponds to lower interfacial energy (Qiu & Zhang, 2013; Zhang, Kelly, Easton & Taylor, 2005; Li *et al.*, 2012; Turnbull & Vonnegut, 1952; Oh *et al.*, 2005; Fan, 2013). In the past, three major geometrical models, *i.e.* linear disregistry (Turnbull & Vonnegut, 1952), planar disregistry (Bramfitt, 1970) and the edge-to-edge matching (E2EM) model (Zhang, Kelly, Qian & Taylor, 2005; Zhang, 2008), have been proposed to quantify the CAM. For example, the E2EM model (Zhang & Kelly, 2005*a*,*b*; Kelly & Zhang, 1999, 2006) has been successfully used to understand the grain refinement mechanism of currently available grain refiners (Qiu, Zhang, Fu *et al.*, 2007; Qiu, Zhang, Taylor, Fu & Kelly, 2007) and the poisoning effect of Si in Al alloys (Qiu, Zhang, Taylor & Kelly, 2007), and to predict new grain refiners for cast metals (Zhang, Kelly, Qian & Taylor, 2005; Qiu, Zhang, Taylor & Kelly, 2009; Fu *et al.*, 2008, 2009; Wang, Qiu *et al.*, 2013; Qiu, Zhang & Kelly, 2009; Qiu & Zhang, 2013; Zhang, Kelly, Easton & Taylor, 2005; Qiu, Zhang, Fu *et al.*, 2007; Jiang *et al.*, 2010). However, atomic matching is only one essential criterion to identify effective grain refiners. The grain refining potency of particles also relies on the particle size and size distribution (Fan *et al.*, 2009; Li *et al.*, 2012; Quested & Greer, 2004), the number density (Easton & StJohn, 2005) and the particle morphology (Qian, 2007; Qiu & Zhang, 2013; Li & Easterling, 1990; Saha, 2010). The free-growth mode, developed by Greer and co-workers (Greer *et al.*, 2000; Quested & Greer, 2004), describes the size effect well. This model is expressed as $\Delta T_{fg} = 4\sigma/(\Delta S_v d_p)$, in which σ, ΔS_v, d_p and ΔT_{fg} are the solid/liquid interfacial energy, the fusion entropy, the particle size and the critical undercooling for free growth, respectively.

In terms of the solute paradigm, the contribution of the solute is associated with solute segregating in front of the solid/liquid (S/L) interface (StJohn *et al.*, 2011; Johnsson *et al.*, 1993; Easton & StJohn, 1999*a*,*b*; Quested & Greer, 2003). For the specified role of solutes in grain refinement, it is generally considered that solute segregation in front of the S/L interface produces a constitutional supercooling (CS) zone (StJohn *et al.*, 2011; Qian *et al.*, 2010; Easton & StJohn, 2001). Such a CS zone provides an additional driving force for new nucleation on potent substrates present. In addition, during the solidification process, the solute segregation at the S/L interface will restrict the growth of the previously formed grains (StJohn *et al.*, 2011; Qian *et al.*, 2010), which subsequently contribute to more nucleation events throughout the bulk of the liquid. For binary alloy systems, the solute effect in grain refinement can be characterized using a growth restriction factor, Q (Easton & StJohn, 2001). The Q value has been widely used to assess the effect of the solute on reducing the grain size (Easton & StJohn, 1999*b*; Maxwell & Hellawell, 1975). Q is defined by

$Q = mc_o(k - 1)$ (Easton & StJohn, 2001), where m, c_o and k are denoted as the liquidus slope, the solute concentration in liquid metal and the partition coefficient. In recent years, the solute paradigm has been extended and, further, the interdependence theory (a Q-value mode) has been proposed (StJohn *et al.*, 2011).

However, there are a number of phenomena that are related to grain refinement in cast metals but cannot be fully explained by a single model/paradigm as mentioned above. Wang, Liu *et al.* (2013) recently reported that, at a constant Q value, the peritectic forming alloying elements (Zr, Nb and V) have much higher grain refining efficiency in cast Al alloys than the eutectic forming elements (Si, Mg and Cu). This was evident, in particular, when the addition level was over the maximum solid solubility. Consequently, it was verified that pro-peritectic compounds, including Al_3Zr (Wang, Liu *et al.*, 2013; Wang, Qiu *et al.*, 2013) and Al_3Nb (Wang *et al.*, 2014), can act as heterogeneous nucleation sites because these particles were observed within Al grains, and reproducible crystallographic orientation relationships were identified. But, Liu *et al.* (2013) found that both peritectic forming alloying elements, such as Ag and Cu, and eutectic forming element, such as Mg and Al, effectively refined cast Zn alloys, even though the four elements have different growth restriction factors in Zn. The authors also reported a new hexagonal close-packed (h.c.p.–h.c.p.) orientation relationship (OR) between $AgZn_3$ and Zn (Liu *et al.*, 2014), indicating the high potency of the pro-peritectic $AgZn_3$ particles as heterogeneous nucleation sites in Zn alloys.

On the basis of these outcomes, it is reasonable to propose a hypothesis that peritectic forming alloying elements have higher grain refining efficiency than eutectic forming elements at the same level of Q value (growth restriction factor). Peritectic reactions may not occur in the practical casting process because of the low mobility of solutes in solids. But, owing to the inherent crystallographic relation between the pro-peritectic phase and the primary solid, the pro-peritectic particles formed directly from liquid can act as effective heterogeneous nucleation sites. The present work aims to further corroborate this hypothesis in the Zn–Cu peritectic system through investigating the effect of Cu addition on grain refinement of cast Zn alloys.

2. Experimental procedure

2.1. Cast sample preparation

Eight Zn alloys with different Cu contents (0.25, 0.5, 1.0, 1.5, 2.0, 2.5, 3.0 and 4.0 wt% Cu) were prepared in a clay-bonded graphite crucible using industrial pure Zn with a purity of 99.995% and Zn–18 wt% Cu master alloy. The crucible was fully coated with boron nitride before use. The master alloy was made by melting the Zn ingot in an argon protective atmosphere and then adding chips of pure Cu with a purity of 99.95%. After melting of the pure Zn in an electrical resistance furnace, various amounts of master alloy were added. Then, the melts were isothermally inoculated for 20 min at 823.15, 873.15, 923.15 and 973.15 K, respectively. After removal of the oxidation skins on top of the melts, they were cast into cylindrical graphite moulds (30 mm in diameter and 40 mm in length), which were pre-heated at the same temperatures as the melts. An N-type thermocouple was inserted into the melt to measure the average cooling rate during solidification. During solidification in air, the cylindrical graphite mould was placed on a 10 mm-thick Fibrefrax board, and then another piece of Fibrefrax board was placed on top of the graphite moulds. This cooling method was developed by Backerud & Shao (1991), and then used by Easton & StJohn (2001) and Wang, Liu *et al.* (2013). The average cooling rates of all castings were around 1 K s^{-1}.

2.2. Microstructural characterization

Metallographic samples were sectioned at approximately 10 mm from the bottom of the as-cast cylindrical ingots. After being mechanically ground and polished, metallographic samples were immersed in the Gennone–Kersey solution (84% distilled water, 15% H_2SO_4 and 1 vol.% HF) for 10 s, and then examined in a Leica optical microscope (OM) using polarized light. In terms of the linear intercept standard (ASTM 112-10), the average grain sizes of as-cast samples were measured using the *Spot32* image analysis software supplied with the Leica OM. Phases in the ingots were identified using X-ray diffraction (XRD), which was performed using a Bruker D8 diffractometer operated at 40 kV with Cu $K\alpha$ radiation (wavelength 1.54056 Å). To further characterize the phases in the samples and to study the crystallography of the pro-peritectic phase, some as-cast samples were examined using a JEOL 7001 high-resolution scanning electron microscopy (HRSEM) apparatus. To help identify the particles in the HESEM images, interesting areas were marked by a micro-indentator in the OM. Chemical compositions of phases were approximated in the JEOL 7001 microscope using energy dispersive spectroscopy (EDS). The EDS instrument was operated at 20 kV.

2.3. Crystallographic investigation

Electron backscattered diffraction (EBSD) was used to determine the OR between the pro-peritectic phase and the η-Zn matrix. Automated EBSD is integrated in the JEOL 7001 instrument, which is also equipped with an Oxford AZtecHKL system. Both EBSD patterns and Euler angles were collected from the pro-peritectic particles and η-Zn matrix. The ORs between the two phases were determined using a recently developed numerical method (Qiu, Zhang & Kelly, 2009) based on the Euler angles.

2.4. Thermal analysis during solidification

In order to better understand the solidification of the Zn–Cu alloys and therefore to clarify the role of the pro-peritectic phase in grain refinement, the thermal analysis technique developed by Backerud & Taminen (1986) was carried out on the alloys with different Cu contents. Before casting, a thermocouple was placed at the centre of the graphite mould with

its tip set at 10 mm from the bottom of the mould. Once the Zn–Cu alloy melts had been cast into the graphite mould, the mould was covered by a Fibrefrax ceramic board lid. The cooling curves were recorded by a data logger and a computer.

3. Results

3.1. Microstructure evolution and characterization

The average grain size (d) variations of the as-cast Zn–Cu alloys with Cu content and inoculation temperature are plotted in Fig. 1. The effect of inoculation temperature is very marginal and, at all inoculation temperatures, the smallest grain is obtained at 2 wt% Cu, which is just over the maximum solubility of Cu in Zn, as illustrated in Fig. 1(*b*). When the Cu content is greater than 2 wt%, grain coarsening occurs at all inoculation temperatures. Taking the samples inoculated at 873.15 K as examples, a representative microstructural evaluation is shown in Fig. 2. As-cast pure Zn has a coarse columnar structure. Addition of 0.5 wt% Cu promotes the formation of equaxed η-Zn grains and refines the columnar

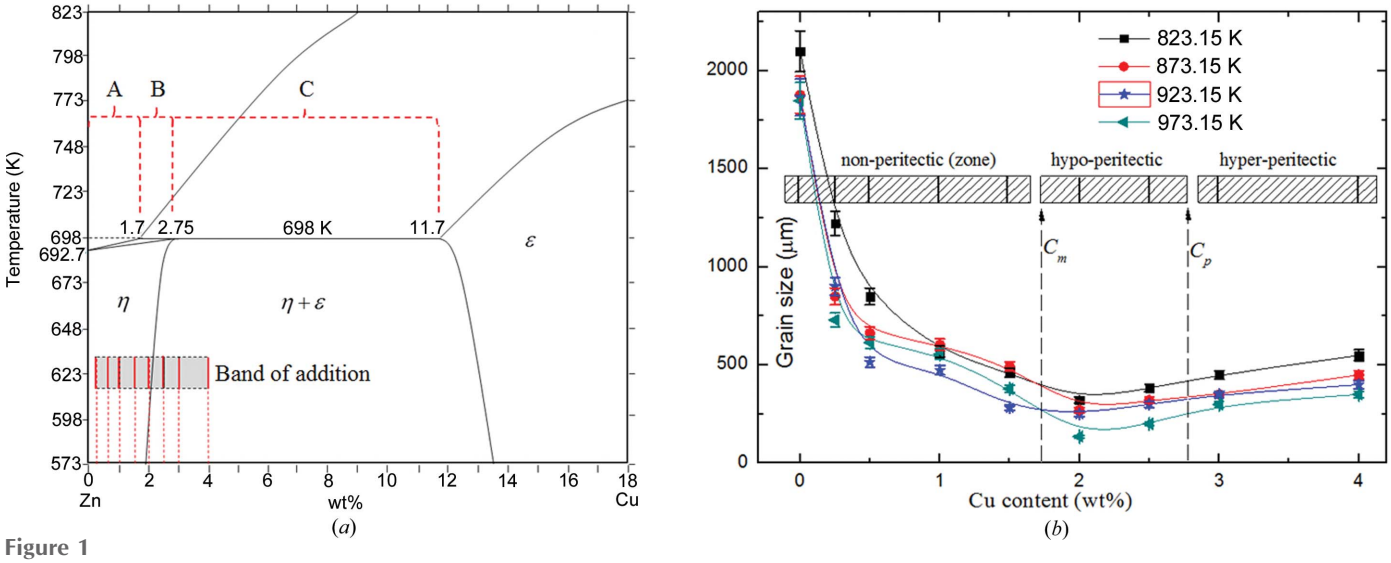

Figure 1
(*a*) Partial Zn–Cu phase diagram (Massalski & King, 1962; Villars, 2006); (*b*) variation of the average grain size with Cu content in the four groups of Zn–Cu alloys inoculated at 823.15, 873.15, 923.15 and 973.15 K, respectively. The shaded bands in (*a*) denote the Cu addition levels in this work. Bands A, B and C in (*a*) correspond to the non-peritectic, hypo-peritectic and hyper-peritectic zones in (*b*), respectively. When the Cu content is over 1.0 wt%, the deviation of grain size measurement is reduced to a relatively small value (for example ±15 μm at 2 wt% Cu), which is covered by the size of the dots. Thus, the error bars are not shown clearly.

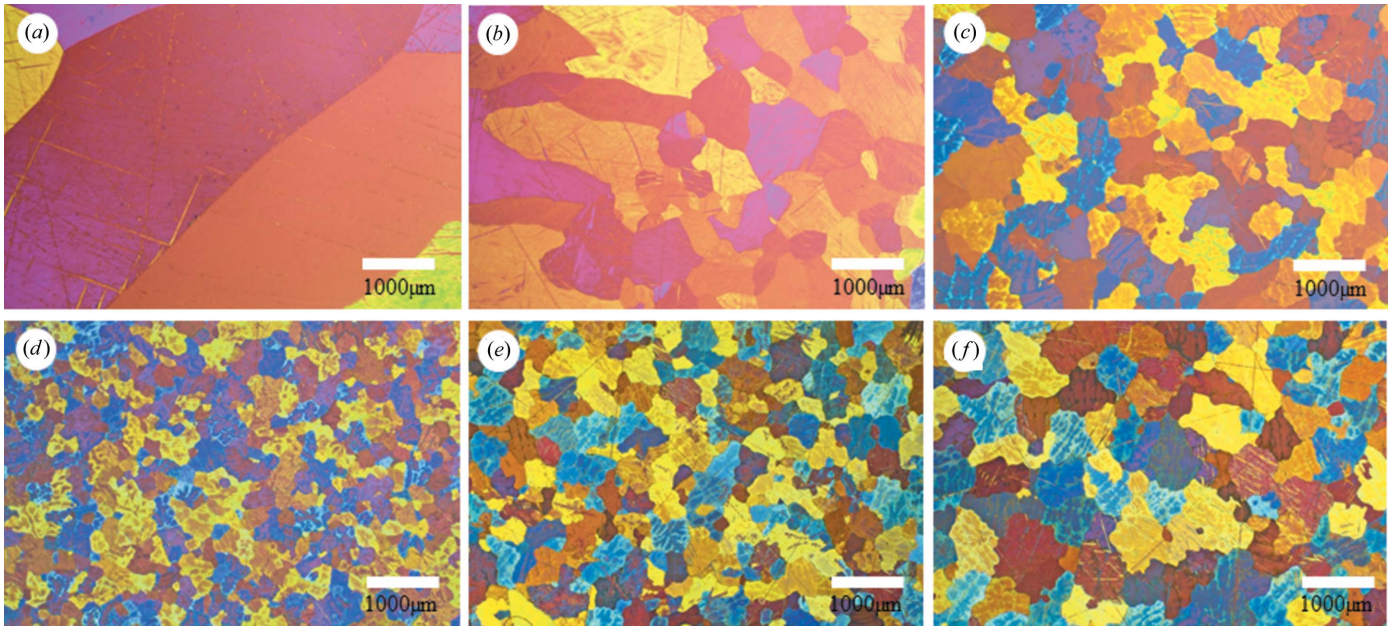

Figure 2
Representative micrographs of the as-cast Zn–Cu binary alloys (all in wt%) inoculated at 873.15 K: (*a*) pure Zn; (*b*) Zn–0.5% Cu; (*c*) Zn–1.0% Cu; (*d*) Zn–2.0% Cu; (*e*) Zn–2.5% Cu; (*f*) Zn–4% Cu.

Table 1
The crystallographic data of Zn and $CuZn_4$ (JCPDS, 2004, 2010).

	Lattice parameters			
Phases	*a* (nm)	*c* (nm)	Person symbol	Space group
Zn	0.26649	0.49468	*hp*2	$P6_3/mmc$
$CuZn_4$	0.27418	0.42939	*hp*2	$P6_3/mmc$

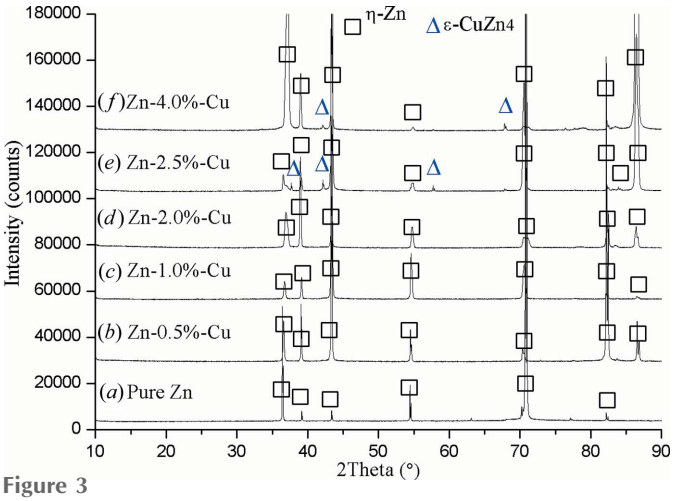

Figure 3
XRD spectra of selected binary cast Zn–Cu alloys, including (*a*) without Cu addition, (*b*) with 0.5% Cu addition, (*c*) with 1.0% Cu addition, (*d*) with 2.0% Cu addition, (*e*) with 2.5% Cu addition and (*f*) with 4.0 wt% Cu addition.

structure. With addition of 1.0 wt% Cu, all of the obtained grains are large and equiaxed, and these grains are further refined with an increase in Cu content. The finest grains are produced at 2 wt% Cu. Grain coarsening occurred when the Cu content was over 2 wt%.

To characterize the phases formed in the alloys, XRD was conducted on all the cast samples. The crystallographic data, including lattice parameters, space group and Person symbol, of η-Zn and ε-$CuZn_4$ are summarized in Table 1. Fig. 3 shows representative XRD spectra of the samples inoculated at 873.15 K. In the alloys containing less than 2 wt% Cu, only η-Zn peaks are observed in spectra (*a*)–(*c*). When the Cu content is over 2 wt%, in addition to the η-Zn peaks, ε-$CuZn_4$ peaks are also detected, as shown in spectra (*e*) and (*f*). ε-$CuZn_4$ was not detected at 2 wt% Cu in (*d*) by XRD because only a small number of particles are present; however, it can be detected using thermal analysis (with details in §4.2). According to the Zn–Cu binary phase diagram (Villars, 2006; David *et al.*, 2003), ε-$CuZn_4$ should be the pro-peritectic phase. To understand the morphology of the pro-peritectic phase, as-cast Zn–2.5 wt% Cu alloys were examined using SEM. Figs. 4(*a*)–4(*b*) show the secondary electron images, demonstrating different intermetallic particles located at or near grain centres, as highlighted by the dashed yellow curves. On the basis of the EDS analysis, the atomic ratio of Cu over Zn was approximately determined to be 1:4.38, as shown in

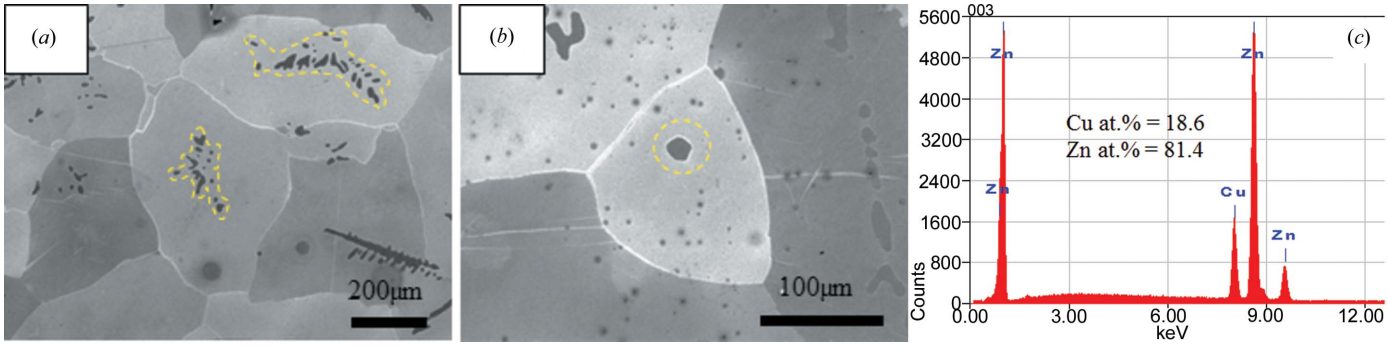

Figure 4
(*a*), (*b*) SEM secondary electron images showing the pro-peritectic $CuZn_4$ particles within the η-Zn grain centres; (*c*) a representative energy dispersive spectrum collected from the particles.

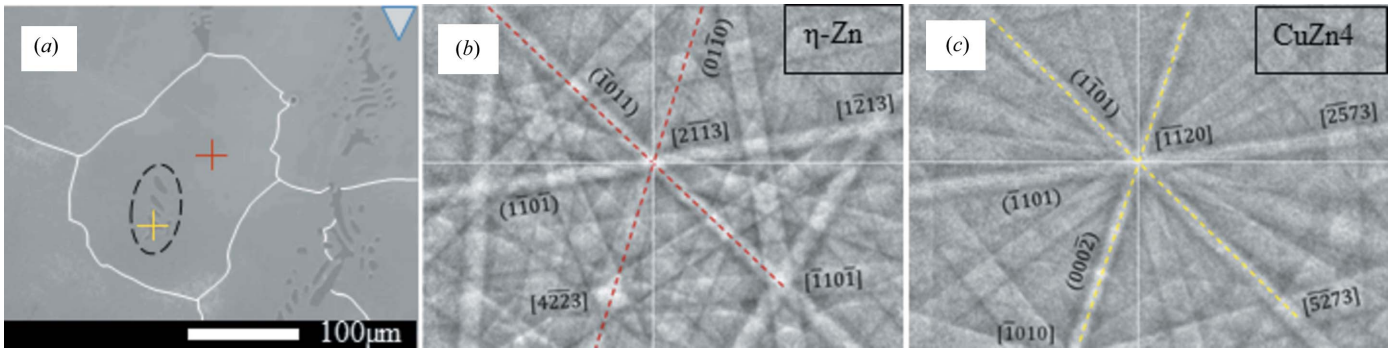

Figure 5
Secondary electron (SE) image of a particle–matrix pair and the corresponding EBSD patterns: (*a*) an SE image of a grain-centred particle (black dashed circle); (*b*) the indexed EBSD pattern taken from the Zn matrix (red dashed lines); (*c*) the indexed EBSD pattern taken from a $CuZn_4$ particle (yellow dashed lines). The grain boundary in (*a*) is highlighted using a white solid line.

Table 2
The ORs between Zn and $CuZn_4$, determined using EBSD combined with an Euler-based numerical method (Qiu & Zhang, 2009).

ORs	Matching directions	Matching planes	Determined frequency
a	$[2\bar{1}\bar{1}3]_{Zn}$ 1.57° away from $[\bar{1}\bar{1}20]_{CuZn4}$	$(01\bar{1}0)_{Zn}$ 0.66° away from $(000\bar{2})_{CuZn4}$ $(\bar{1}011)_{Zn}$ 1.50° away from $(1\bar{1}01)_{CuZn4}$	5/33
b	$[\bar{1}\bar{1}20]_{Zn}$ 1.98° away from $[\bar{2}110]_{CuZn4}$	$(\bar{1}011)_{Zn}$ 1.37° away from $(\bar{1}\bar{1}01)_{CuZn4}$ $(1\bar{1}00)_{Zn}$ 2.03° away from $(0\bar{1}10)_{CuZn4}$	2/33
c	$[\bar{1}2\bar{1}0]_{Zn}$ 2.32° away from $[11\bar{2}0]_{CuZn4}$	$(10\bar{1}1)_{Zn}$ 2.89° away from $(0002)_{CuZn4}$ $(\bar{1}011)_{Zn}$ 11.3° away from $(\bar{1}10\bar{1})_{CuZn4}$	1/33
d	$[\bar{1}2\bar{1}0]_{Zn}$ 4.93° away from $[11\bar{2}\bar{3}]_{CuZn4}$	$(0002)_{Zn}$ 4.81° away from $(1\bar{1}00)_{CuZn4}$ $(10\bar{1}\bar{1})_{Zn}$ 6.23° away from $(10\bar{1}\bar{1})_{CuZn4}$	1/33

Fig. 4(*c*), which is very close to the reported $Cu_{0.2}Zn_{0.8}$ phase (Villars, 2006; David *et al.*, 2003). This is also consistent with the XRD results. However, the particles possess two different morphologies. One is the dendrite shape as shown in Fig. 4(*a*), which is similar to those observed in the Zn–Ag alloys (Liu *et al.*, 2014), and the other has a regular shape as shown in Fig. 4(*b*). It is believed that both particles are the pro-peritectic ε-$CuZn_4$.

3.2. Orientation relationships between $CuZn_4$ and η-Zn

To correlate the formation of pro-peritectic particles with the variation in grain size of the as-cast Zn–Cu alloys, crystallographic ORs between the grain-centred ε-$CuZn_4$ particles and η-Zn matrix were determined using a numerical method based on the EBSD technique, which was developed by Qiu, Zhang & Kelly (2009). In total, 33 pairs of η-Zn matrix and ε-$CuZn_4$ particle were examined. A representative secondary electron image of a particle–matrix pair and the corresponding EBSD patterns are shown in Fig. 5. This pair of EBSD patterns shows that the $[2\bar{1}\bar{1}3]_{Zn}$ and $[\bar{1}\bar{1}20]_{CuZn4}$ Kikuchi poles are close to each other, and the $(\bar{1}011)_{Zn}$ and $(01\bar{1}0)_{Zn}$ Kikuchi bands are nearly parallel to $(1\bar{1}01)_{CuZn4}$ and $(000\bar{2})_{CuZn4}$, respectively. Within these 33 particle (ε-$CuZn_4$) and matrix (η-Zn) pairs, four ORs that have crystallographic meanings were determined. They are named as OR(*a*), OR(*b*), OR(*c*) and OR(*d*) as listed in Table 2. The occurring frequencies of OR(*a*), OR(*b*), OR(*c*) and OR(*d*) are 5/33, 2/33, 1/33 and 1/33, respectively. Other particles (24 out of 33) examined had no crystallographic relation with the η-Zn matrix. The reproducible OR(*a*), together with the predicted OR from the E2EM model (more details are given in §4.1), are also expressed in a stereographic projection, as shown in Fig. 6. It can be seen that the experimentally determined OR agrees well with the E2EM predictions.

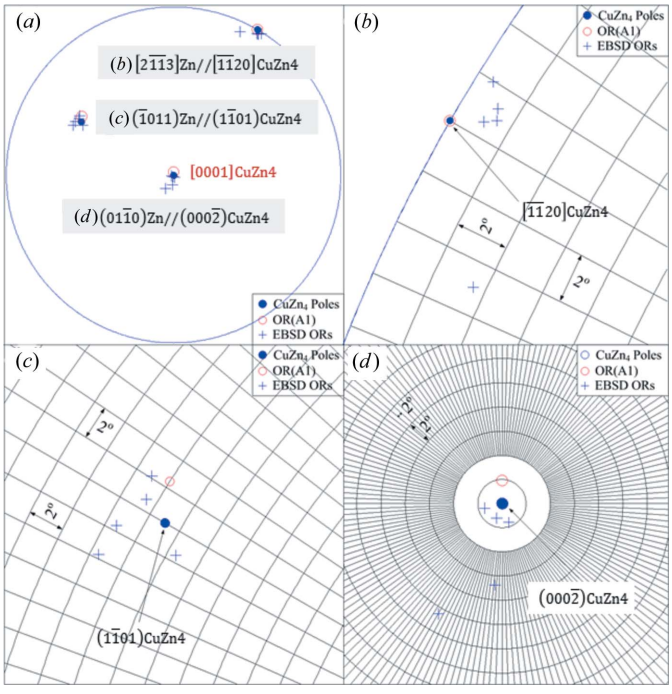

Figure 6
Stereographic projection demonstrating the EBSD-determined OR(*a*) and the corresponding E2EM model-predicted OR(1), plotted in terms of h.c.p. $CuZn_4$ in the $[0001]_{CuZn4}$ direction. Three portions of the projection in terms of OR(*a*) are enlarged in (*b*)–(*d*).

4. Discussion

4.1. Nucleation crystallography in the refined Zn–Cu alloys

The crystallographic relation between the pro-peritectic ε-$CnZn_4$ particles and the η-Zn matrix indicates the high probability that the η-Zn grains nucleated on the pro-peritectic particles through either heterogeneous nucleation or peritectic reaction. Those particles (24 out of 33) that have no crystallographic relation with the η-Zn matrix were highly likely enclosed within the grains during grain growth. In those grains, the sectioning plane just missed the nucleation particles. To further clarify the potency of the ε-$CuZn_4$ particles as heterogeneous nucleation sites for η-Zn, their crystallography was studied. From a crystallographic point of view, the nucleation potency is proportional to the reciprocal of the disregistry between nucleant and grains (Turnbull & Vonnegut, 1952). According to the E2EM model (Zhang, Kelly, Qian & Taylor, 2005; Zhang, Kelly, Easton & Taylor, 2005; Zhang, 2008), nucleants with high efficiency correspond to low interatomic misfit (f_r) along matching directions and small interplanar mismatch (f_d) between matching planes with the grains. In the present work, η-Zn has an h.c.p. crystal structure with a = 0.26649 nm, c = 0.49468 nm and Person symbol *hp*2, belonging to space group $P6_3/mmc$ (JCPDS, 2004). ε-$CuZn_4$ also has a simple h.c.p. structure (equivalent to Cu_4Zn; David *et al.*, 2003; JCPDS, 2010). Its lattice parameters are a = 0.27418 nm and c = 0.42939 nm with Person symbol *hp*2 and space group $P6_3/mmc$. Zn comprises three close-packed (c.p.) plane families, $\{0002\}_{Zn}$, $\{1\bar{1}01\}_{Zn}$ and $\{\bar{2}110\}_{Zn}$, and three c.p. direction families, $\langle 2\bar{1}\bar{1}0\rangle^{SS}_{Zn}$, $\langle\bar{1}2\bar{1}3\rangle^{PS}_{Zn}$ and $\langle 10\bar{1}0\rangle^{ZZ}_{Zn}$. Here the superscripts, S, PS and ZZ refer to straight, pseudo-straight and zigzag atomic rows, respectively (Zhang, Kelly, Qian & Taylor, 2005; Zhang, Kelly, Easton & Taylor,

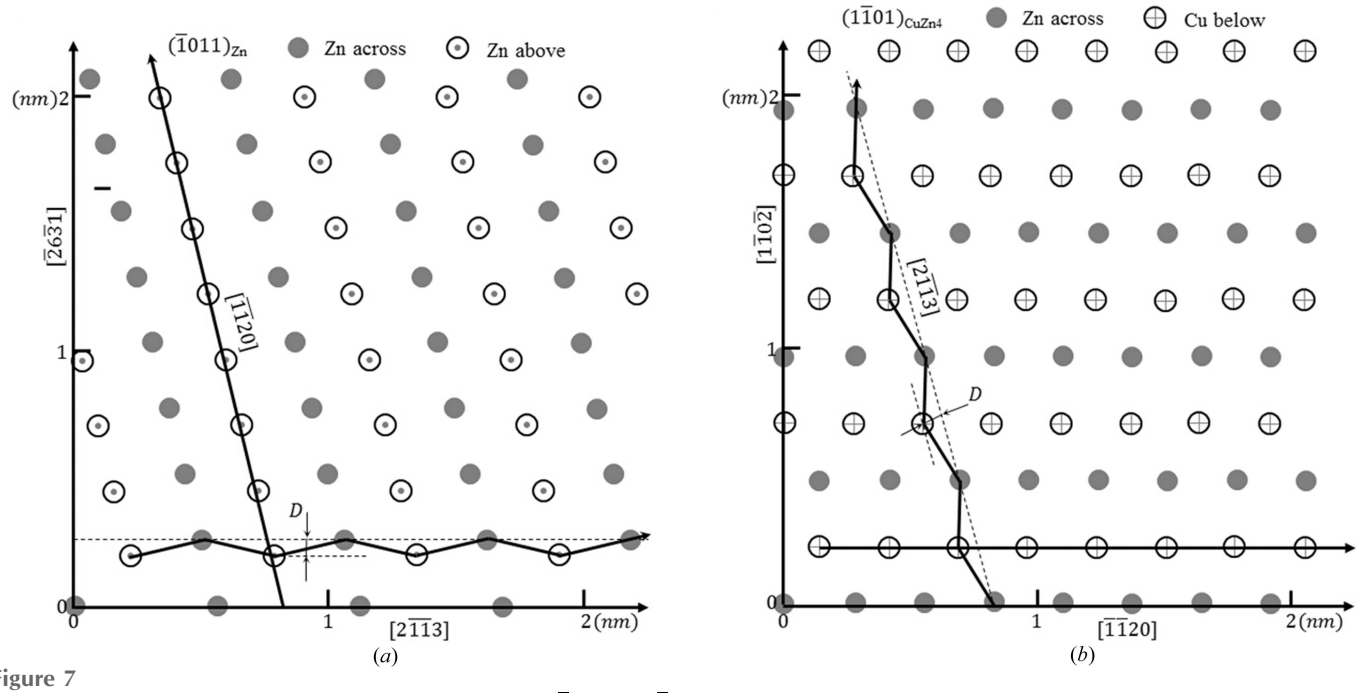

Figure 7
Schematic atomic configuration on one matching plane pair, $(\bar{1}011)_{Zn}//(1\bar{1}01)_{CuZn4}$. The bold lines, representing close-packed atomic rows, demonstrate the matching directions within matching planes. The offline distance, D, for an atom relative to the matching planes is no more than an atomic radius (Zhang, Kelly, Qian & Taylor, 2005; Zhang, Kelly, Easton & Taylor, 2005).

2005). ε-$CuZn_4$ possesses four c.p. plane families, $\{0002\}_{CuZn4}$, $\{1\bar{1}01\}_{CuZn4}$, $\{\bar{2}110\}_{CuZn4}$ and $\{10\bar{1}0\}_{CuZn4}$, and two c.p. direction families, $\langle 2\bar{1}\bar{1}0\rangle^{SS}_{CuZn4}$ and $\langle \bar{1}2\bar{1}3\rangle^{PS}_{CuZn4}$.

On the basis of the E2EM model through calculation of the f_r and f_d values, a total of five ORs are predicted, which are listed in Table 3. The E2EM model-predicted ORs (1), (2), (3) and (4) agree well with the EBSD-determined ORs (*a*), (*b*), (*c*) and (*d*), respectively, listed in Table 2. Fig. 7 schematically illustrates the atomic configurations on two matching planes $(\bar{1}011)_{Zn}//(1\bar{1}01)_{CuZn4}$, which are associated with the predicted OR(1) [or determined OR(*a*)]. The atomic configuration of the c.p. $(\bar{1}011)_{Zn}$ plane, containing the c.p. $[\bar{1}\bar{1}20]^{SS}_{Zn}$ and $[2\bar{1}\bar{1}3]^{PS}_{Zn}$ directions, is demonstrated in Fig. 7(*a*). The atomic configuration of the c.p. $(1\bar{1}01)_{CuZn4}$ plane, containing the c.p. $[2\bar{1}\bar{1}3]^{PS}_{CuZn4}$ and $[\bar{1}\bar{1}20]^{SS}_{CuZn4}$ directions, is shown in Fig. 7(*b*). Atomic configurations on other matching planes can also be constructed. For brevity, they are not shown here. Fig. 8 shows simulated superimposed diffraction patterns along the $[2\bar{1}\bar{1}3]_{Zn}/[\bar{1}\bar{1}20]_{CuZn4}$ zone axis, illustrating the predicted OR(1) between Zn and $CuZn_4$, which corresponds to the experimentally determined OR(*a*) in Fig. 5. The simulated rotation angles between two matching plane pairs, *i.e.* $(\bar{1}011)_{Zn}/(1\bar{1}01)_{CuZn4}$ and $(01\bar{1}0)_{Zn}/(000\bar{2})_{CuZn4}$, are 0.31 and 1.69°,

Table 3
The interatomic spacing misfit (f_r) along matching directions, interplanar spacing mismatch (f_d) between matching planes, and E2EM model-predicted ORs between Zn and $CuZn_4$.

ORs	Matching directions	f_r (%)	Matching planes	f_d (%)
1	$[2\bar{1}\bar{1}3]_{Zn}//[\bar{1}\bar{1}20]_{CuZn4}$	2.47	$(\bar{1}011)_{Zn}$ 0.31° away from $(1\bar{1}01)_{CuZn4}$	0.65
			$(01\bar{1}0)_{Zn}$ 1.69° away from $(000\bar{2})_{CuZn4}$	
2	$[2\bar{1}\bar{1}0]_{Zn}//[2\bar{1}\bar{1}0]_{CuZn4}$	2.80	$(0\bar{1}\bar{1}1)_{Zn}$ 0.30° away from $(0\bar{1}\bar{1}1)_{CuZn4}$	0.65
			$(0\bar{1}10)_{Zn}$ 3.63° away from $(0\bar{1}10)_{CuZn4}$	
3	$[\bar{1}2\bar{1}0]_{Zn}//[11\bar{2}0]_{CuZn4}$	2.80	$(\bar{1}011)_{Zn}$ 0.19° away from $(\bar{1}10\bar{1})_{CuZn4}$	0.65
			$(10\bar{1}1)_{Zn}$ 10.85° away from $(0002)_{CuZn4}$	2.58
4	$[\bar{1}2\bar{1}0]_{Zn}//[11\bar{2}3]_{CuZn4}$	4.62	$(0002)_{Zn}$ 0.42° away from $(1\bar{1}00)_{CuZn4}$	4.17
			$(10\bar{1}1)_{Zn}$ 1.35° away from $(10\bar{1}\bar{1})_{CuZn4}$	0.65
5	$[\bar{2}113]_{Zn}//[2\bar{1}\bar{1}0]_{CuZn4}$	2.47	$(\bar{1}01\bar{1})_{Zn}$ 1.05° away from $(000\bar{2})_{CuZn4}$	2.58
			$(0\bar{1}10)_{Zn}$ 3.05° away from $(01\bar{1}1)_{CuZn4}$	

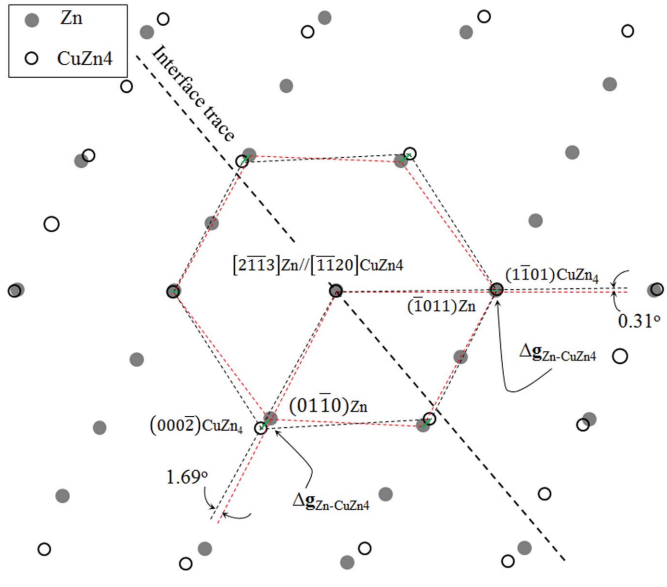

Figure 8
Simulated diffraction patterns of the EBSD-determined OR(*a*) in Fig. 5 along the $[2\bar{1}\bar{1}3]_{Zn}/[\bar{1}\bar{1}20]_{CuZn4}$ zone axis. The rotation angles between two matched plane pairs are 0.31 and 1.69°, respectively. All $\Delta\mathbf{g}$s are perpendicular to the interface trace (dashed line).

respectively. These two simulated angles are very close to the determined values (0.66 and 1.50°).

Previous work (Qiu, Zhang, Taylor & Kelly, 2009; Fu *et al.*, 2009; Wang, Qui *et al.*, 2013; Fan *et al.*, 2009; Qiu & Zhang, 2013; Li *et al.*, 2012; Liu *et al.*, 2014; Zeng *et al.*, 2014) verifies that low f_r and f_d values are associated with a high nucleation potency of primary solids on the particles. Generally, for an effective nucleant, the values of f_r and f_d are lower than 7%. Examples include Mg–AlN (Fu *et al.*, 2009), Mg–Al_2Y (Qiu, Zhang, Taylor & Kelly, 2009; Qiu & Zhang, 2013), Mg–Zr (Li *et al.*, 2012; Saha, 2010), Mg–MgO (Fan *et al.*, 2009), Al–Al_3Zr (Wang, Qiu *et al.*, 2013), Al–Al_3Nb (Wang *et al.*, 2014), Zn–$AgZn_3$ (Liu *et al.*, 2014) and Li–$Mg_{24}Y_5$ (Zeng *et al.*, 2014) systems. Regarding the present Zn–$CuZn_4$ system, the f_r and f_d values related to all matching directions and matching planes were calculated on the basis of the E2EM model; they are listed in Table 3. It can be seen that both f_r and f_d values are smaller than 5% for all possible ORs. The above analysis indicates that $CuZn_4$ can act as potent heterogeneous nucleation sites for η-Zn grains.

4.2. Effect of the pro-peritectic particle size and Cu solute on grain refinement

On the basis of the above discussions, ε-$CuZn_4$ can be considered as a potent heterogeneous nucleation site for η-Zn, leading to grain refinement. However, the experimental results in Fig. 1(*b*) show grain coarsening when the Cu content is over 2 wt%, even though more of the pro-peritectic ε-$CuZn_4$ phase formed in the Zn alloys with high Cu content. This phenomenon can be explained through correlating the growth restriction factor (Q value) with the particle size effect on the heterogeneous nucleation. Compared with other well acknowledged grain refining solutes that have high Q values (at the maximum solubility), such as Q(Ti) = 33 K in Al (Easton & StJohn, 2001), Q(Zr) = 13.6 K in Mg (StJohn *et al.*, 2005), Q(B) = 15 K in Ti (Bermingham *et al.*, 2008) and Q(Ag) = 19.1 K in Zn (Liu *et al.*, 2014), the Q value of Cu in Zn corresponding to the maximum solubility (1.7 wt%) is much smaller (3.4 K) (Liu *et al.*, 2013). This implies that Cu solute has a limited restriction effect on η-Zn grain growth. In addition, according to the empirical equation (1) proposed by Easton and StJohn (Easton & StJohn, 2001, 2008; StJohn *et al.*, 2007), the average grain size of cast metals should be linearly proportional to the reciprocal of the Q value, $1/Q$:

$$d = \frac{a}{(\rho_v f)^{1/3}} + \frac{D\Delta T_n}{vQ}, \qquad (1)$$

where a, ρ_v, f, v and ΔT_n represent a fitting coefficient, the density of nucleant particles, the fraction of active nucleant particles, the growth velocity of grains and the critical undercooling for nucleation, respectively. D is the diffusion coefficient of the solute element in liquid metal. These parameters depend on specified grain-refining alloy systems (Easton & StJohn, 2008; StJohn *et al.*, 2007). However, on plotting the average grain size of Zn–Cu alloys that were cast at a cooling rate of 1 K s^{-1} as a function of $1/Q$ (when the Cu content is greater than the maximum solubility, C_m, the Q values were calculated using C_m; Wang, Liu *et al.*, 2013) as shown in Fig. 9(*a*), a nonlinear relation is obtained. This implies that there are other factors that influence the grain size.

In order to understand the solidification process of Zn–Cu alloys in more depth, a thermal analysis was carried out on the binary Zn alloys with various Cu contents. Fig. 10 contains

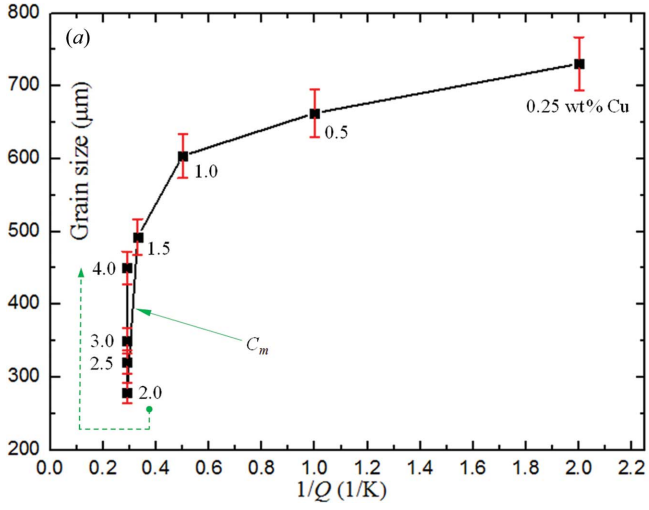

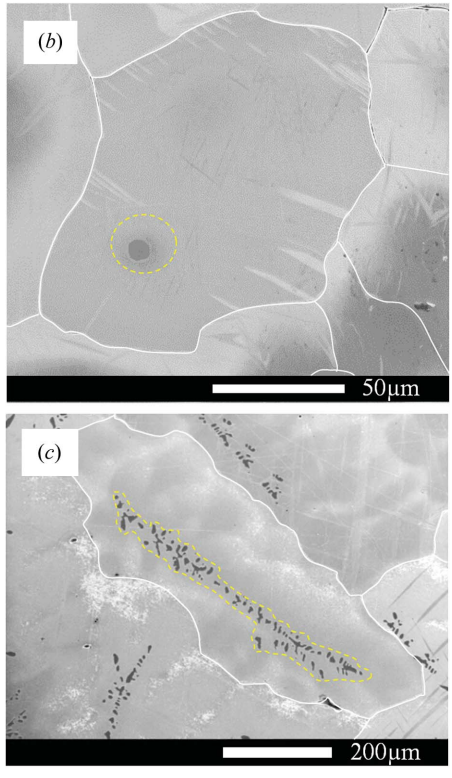

Figure 9
(*a*) The average grain sizes of Zn–Cu alloys plotted as a function of the reciprocal of the growth restriction factor, $1/Q$; (*b*) a small ε-$CuZn_4$ particle observed in the Zn–2 wt% Cu alloy; (*c*) large dendrite ε-$CuZn_4$ particles observed in the Zn–4wt% Cu alloy.

representative thermal analysis results of binary Zn alloys with Cu contents of 1.0, 2.0, 2.5 and 4.0 wt%, showing both the cooling curves and the variations of cooling rate with cooling time during solidification. Any slope change on the cooling curves corresponds to a phase transformation. This can be more clearly illustrated by the cooling rate curves. When the Cu content is below the maximum solubility, C_m, as shown in Fig. 10(*a*), there is only one broad peak on the cooling rate curve staring at 697.16 K, which is below the peritectic temperature (698 K) of the Zn–Cu system. This peak corresponds to the formation of η-Zn directly from the liquid. Once the Cu content is over C_m, as shown in Figs. 10(*b*)–10(*d*), a narrow peak appears before the broad peak on the cooling rate curves. According to the Zn–Cu phase diagram, this narrow peak corresponds to the formation of the ε-$CuZn_4$ phase from the liquid. With increasing Cu content from 2.0 to 4.0 wt%, the formation temperature of the ε-$CuZn_4$ phase increases from 707.44 to 766.69 K. This is consistent with the Zn–Cu phase diagram. As a result of forming ε-$CuZn_4$ from the liquid, the formation temperatures of η-Zn rise to 699.78 K at 2.0 wt% Cu and 700.20 K at 2.5 and 4.0 wt% Cu, respectively. This implies that ε-$CuZn_4$ promoted the formation of η-Zn at temperatures above the peritectic temperature. Although further evidence is required, it is highly likely that the η-Zn in the alloys with Cu content over C_m formed through heterogeneous nucleation on the pro-peritectic ε-$CuZn_4$ phase. This is due to three reasons. (1) As stated above, ε-$CuZn_4$ can act as effective heterogeneous nucleation sites for η-Zn. (2) Because the actual cooling rate during thermal analysis was much higher than the ideal equilibrium cooling rate, which is considered as indefinitely slow, the peritectic reaction is unlikely to occur because of the too slow diffusion of solute into the solid (Qian & Das, 2006; StJohn, 1990; StJohn & Qian, 2009). (3) Provided the peritectic reaction occurred, it should commence at or below the peritectic temperature of 698 K; however, Fig. 10 shows that η-Zn started forming at a higher temperature. From Fig. 10, it also can be seen that the Cu content increases the ε-$CuZn_4$ growth time before the nucleation of η-Zn. The ε-$CuZn_4$ growth time is defined as the time difference between the formation of the ε-$CuZn_4$ phase and the η-Zn phase, as shown by Δt in Figs. 10(*b*)–10(*d*). Therefore, in contrast to the small ε-$CuZn_4$ particles at low Cu content as shown in Fig. 9(*b*), large dendritic ε-$CuZn_4$ particles formed and were observed in the alloys with high Cu content, as revealed in Fig. 9(*c*). According to the free growth model (Greer *et al.*, 2000; Quested & Greer, 2004), larger particles can more effectively promote heterogeneous nucleation.

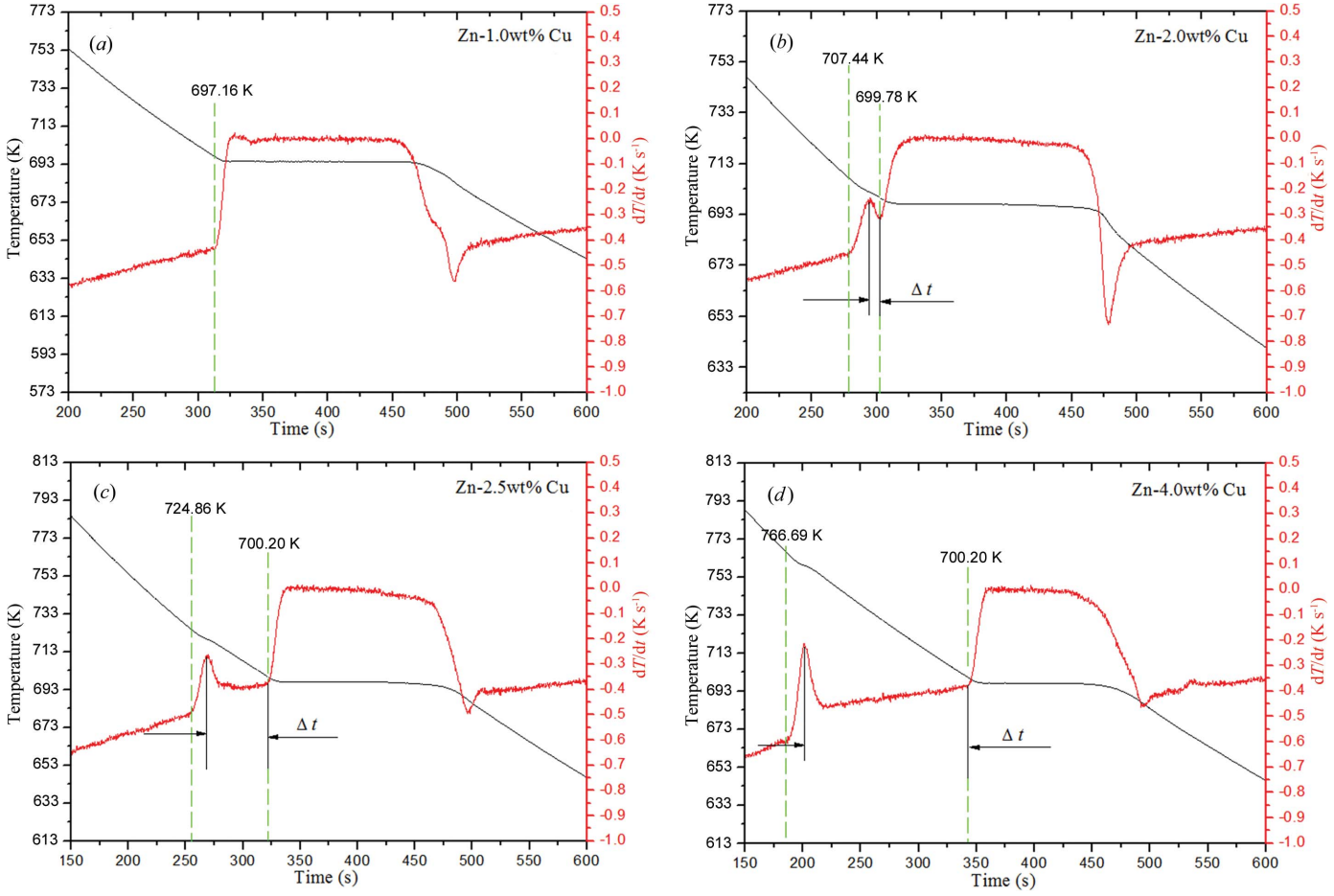

Figure 10
Cooling curves and cooling rate curves determined from thermal analysis on (*a*) 1.0 wt% Cu, (*b*) 2.0 wt% Cu, (*c*) 2.5 wt% Cu and (*d*) 4.0 wt% Cu. Δt in (*b*)–(*d*) is the growth time of the pro-peritectic ε-$CuZn_4$ phase before the formation of η-Zn.

On the basis of the above crystallographic discussions and the thermal analysis outcomes, the results shown in Figs. 1 and 2 can be explained as follows. When the Cu content is below C_m (1.7 wt%), no pro-peritectic phase forms. η-Zn can only nucleate on either native nucleant particles (if they exist in the Zn melt) or mould walls at temperatures below the peritectic temperature. In this case, although the Q value of Cu in Zn is small, it still restricts the grain growth compared with pure Zn, particularly at lower temperatures. Hence, an increase in Cu content leads to smaller grains. At a Cu content of 2.0 wt%, which is just over C_m, a small fraction of ε-$CuZn_4$ phase forms before η-Zn nucleates. Because of the small amount, the ε-$CuZn_4$ particles formed are small. Heterogeneous nucleation on such ε-$CuZn_4$ particles positively contributes to the grain refinement. Hence, the smallest grain size is obtained at 2.0 wt% Cu. Once the Cu content is over 2 wt%, coarse ε-$CuZn_4$ dendrites form within the liquid prior to the formation of η-Zn. Such large ε-$CuZn_4$ particles act as preferred and effective heterogeneous nucleation sites for η-Zn. Because the total fraction of the pro-peritectic $CuZn_4$ phase is defined by the phase diagram, larger particles are associated with small numbers in terms of a fixed cast volume. Thus, the overall number of nuclei formed through heterogeneous nucleation is lowered. Furthermore, owing to the low Q value of Cu (limited restriction on grain growth) and relatively higher temperature, the growth velocity of η-Zn grains nucleated on the pro-peritectic particles is high. This results in grain coarsening. In summary, heterogeneous nucleation in liquid metals does not have to lead to grain refinement. It depends on the number and size of the heterogeneous nucleation sites (normally called nucleants) and the restriction effect of solutes on grain growth.

5. Conclusions

(1) Addition of Cu can effectively convert a columnar structure into equiaxed grains and significantly refine the grain size of cast Zn–Cu alloys. The smallest grains are produced at 2.0 wt% Cu. Further addition of Cu led to coarsening of $CuZn_4$ particles, resulting in a decrease in the number density of the potent nucleant particles. In addition, owing to the low growth restriction factor (Q value) of Cu in liquid Zn, the higher Cu content had a limited effect on restriction of grain growth. Hence, the grain size increased in the Zn–Cu alloy when the Cu content was over 2.0 wt%.

(2) A reproducible h.c.p.–h.c.p. OR between the pro-peritectic ε-$CuZn_4$ phase and η-Zn was experimentally determined in the grain-refined Zn–Cu alloys. This OR can be expressed as $[2\bar{1}\bar{1}3]_{Zn}//[\bar{1}\bar{1}20]_{CuZn4}$, $(\bar{1}011)_{Zn}//(1\bar{1}01)_{CuZn4}$, $(01\bar{1}0)_{Zn}//(000\bar{2})_{CuZn4}$. This indicates that the pro-peritectic ε-$CuZn_4$ particles can act as potent heterogeneous nucleation sites for η-Zn grains regardless of whether the peritectic reaction occurs or not.

(3) Heterogeneous nucleation in liquid metals does not definitely result in grain refinement. It depends on the number and size of the heterogeneous nucleation sites (normally called nucleant particles) and the restriction effect of solutes on grain growth.

Acknowledgements

Grateful acknowledgement is expressed to the Australian Research Council for funding support. ZL is indebted to the China Scholarship Council and The University of Queensland for providing a scholarship. Both the Centre for Microscopy and Microanalysis (CMM) at the University of Queensland and the Central Analytical Research Facility (CARF) at Queensland University of Technology are appreciated for facilities and assistance.

References

Backerud, L. & Shao, Y. (1991). *Aluminium (Germany)*, **67**, 780–785.
Backerud, L. K. & Taminen, J. (1986). *Solidification Characteristics of Aluminium Alloys.* Oslo: Universitetsforlaget AS.
Banerji, A., Feng, Q. L. & Reif, W. (1989). *Metall. Trans. A*, **20**, 564–566.
Barker, N. J. W. & Hellawell, A. (1974). *Met. Sci.* **8**, 353–356.
Bermingham, M. J., McDonald, S. D., Dargusch, M. S. & StJohn, D. H. (2008). *Scr. Mater.* **58**, 1050–1053.
Bramfitt, B. L. (1970). *Metall. Trans.* **1**, 1987–1995.
Chen, S. W., Chen, C. C., Gierlotka, W., Zi, A. R., Chen, P. & Wu, H. (2008). *J. Elec. Mater.* **37**, 992–1002.
Crosley, F. A. & Mondolfo, L. F. (1951). *AIME Trans.* **191**, 1143–1150.
David, N., Fiorani, J. M., Vilasi, M. & Hertz, J. (2003). *J. Phase Equilib.* **24**, 240–248.
Davies, I., Dennis, J. & Hellawell, A. (1970). *Met. Mater. Trans. B*, **1**, 275–280.
Easton, M. A., Schiffl, A., Yao, J. Y. & Kaufmann, H. (2006). *Scr. Mater.* **55**, 379–382.
Easton, M. & StJohn, D. H. (1999*a*). *Metall. Mater. Trans. A*, **30**, 1613–1623.
Easton, M. & StJohn, D. H. (1999*b*). *Metall. Mater. Trans. A*, **30**, 1625–1633.
Easton, M. A. & StJohn, D. H. (2001). *Acta Mater.* **49**, 1867–1878.
Easton, M. & StJohn, D. H. (2005). *Metall. Mater. Trans. A*, **36**, 1911–1920.
Easton, M. A. & StJohn, D. H. (2008). *Mater. Sci. Eng. A*, **486**, 8–13.
Emley, E. F. (1966). *Principles of Magnesium Technology.* Oxford: Pergamon Press.
Exner, H. E. & Petzow, G. (1985). *Metals Handbook*, 9th ed., Vol. 9, pp. 675–680. Materials Park: ASM International.
Fan, Z. (2013). *Metall. Mater. Trans. A*, **44**, 1409–1418.
Fan, Z., Wang, Y., Xia, M. & Arumuganathar, S. (2009). *Acta Mater.* **57**, 4891–4901.
Fu, H. M., Qiu, D., Zhang, M. X., Wang, H., Kelly, P. M. & Taylor, J. A. (2008). *J. Alloys Compd.* **456**, 390–394.
Fu, H. M., Zhang, M. X., Qiu, D., Kelly, P. M. & Taylor, J. A. (2009). *J. Alloys Compd.* **478**, 809–812.
Glardon, R. & Kurz, W. (1981). *J. Cryst. Growth*, **51**, 283–291.
Greer, A. L., Bunn, A. M., Tronche, A., Evans, P. V. & Bristow, D. J. (2000). *Acta Mater.* **48**, 2823–2835.
Greer, A. L., Cooper, P. S., Meredith, M. W., Schneider, W., Schumacher, P., Spittle, J. A. & Tronche, A. (2003). *Adv. Eng. Mater.* **5**, 81–91.
Izumi, T., Nakamura, Y. & Shiohara, Y. (1993). *J. Cryst. Growth*, **128**, 757–761.
JCPDS (2004). JCPDS No. 01-073-6858. Joint Committee on Powder Diffraction Standards–International Centre for Diffraction Data, Newtown Square, PA, USA.

JCPDS (2010). JCPDS No. 01-071-7925. Joint Committee on Powder Diffraction Standards–International Centre for Diffraction Data, Newtown Square, PA, USA
Jiang, B., Qiu, D., Zhang, M. X., Ding, P. D. & Gao, L. (2010). *J. Alloys Compd.* **492**, 95–98.
Johnsson, M., Backerud, L. & Sigworth, G. K. (1993). *Metall. Trans. A*, **24**, 481–491.
Kelly, P. M. & Zhang, M. X. (1999). *Mater. Forum*, **23**, 41–62.
Kelly, P. M. & Zhang, M. X. (2006). *Metall. Mater. Trans. A*, **37**, 833–839.
Lee, Y. C., Dahle, A. K. & StJohn, D. H. (2000). *Metall. Mater. Trans. A*, **31**, 2895–2906.
Li, H. T., Wang, Y. & Fan, Z. (2012). *Acta Mater.* **60**, 1528–1537.
Li, W. B. & Easterling, K. E. (1990). *Acta Metall. Mater.* **38**, 1045–1052.
Liu, Z. L., Qiu, D., Wang, F., Taylor, J. A. & Zhang, M. X. (2014). *Acta Mater.* **79**, 315–326.
Liu, Z. L., Wang, F., Qiu, D., Taylor, J. A. & Zhang, M. X. (2013). *Metall. Mater. Trans. A*, **44**, 4025–4030.
Massalski, T. B. & King, H. W. (1962). *Acta Metall.* **10**, 1171–1181.
Maxwell, I. & Hellawell, A. (1975). *Acta Metall.* **23**, 229–237.
McCartney, D. G. (1989). *Int. Mater. Rev.* **34**, 247–260.
McDonald, N. J. & Sridhar, S. (2003). *Metall. Mater. Trans. A*, **34**, 1931–1940.
Mohanty, P. S. & Gruzleski, J. E. (1995). *Acta Metall. Mater.* **43**, 2001–2012.
Murty, B. S., Kori, S. A. & Chakraborty, M. (2002). *Int. Mater. Rev.* **47**, 3–29.
Oh, S. H., Kauffmann, Y., Scheu, C., Kaplan, W. D. & Rühle, M. (2005). *Science*, **310**, 661–663.
Qian, M. (2007). *Acta Mater.* **55**, 943–953.
Qian, M., Cao, P., Easton, M. A., McDonald, S. D. & StJohn, D. H. (2010). *Acta Mater.* **58**, 3262–3270.
Qian, M. & Das, A. (2006). *Scr. Mater.* **54**, 881–886.
Qian, M., Ramirez, A. & Das, A. (2009). *J. Cryst. Growth*, **311**, 3708–3715.
Qiu, D. & Zhang, M. X. (2009). *J. Alloys Compd.* **488**, 260–264.
Qiu, D. & Zhang, M. X. (2013). *J. Alloys Compd.* **586**, 39–44.
Qiu, D., Zhang, M. X., Fu, H. M., Kelly, P. M. & Taylor, J. A. (2007). *Acta Mater.* **87**, 505–514.
Qiu, D., Zhang, M. X. & Kelly, P. M. (2009). *Scr. Mater.* **61**, 312–315.
Qiu, D., Zhang, M. X., Taylor, J. A., Fu, H. M. & Kelly, P. M. (2007). *Acta Mater.* **55**, 1863–1871.
Qiu, D., Zhang, M. X., Taylor, J. A. & Kelly, P. M. (2007). *Acta Mater.* **55**, 1447–1456.
Qiu, D., Zhang, M. X., Taylor, J. A. & Kelly, P. M. (2009). *Acta Mater.* **57**, 3052–3059.
Quested, T. E. & Greer, A. L. (2003). *Light Met.* **2003**, 945–952.
Quested, T. E. & Greer, A. L. (2004). *Acta Mater.* **52**, 3859–3868.
Saha, P. (2010). PhD thesis, The University of Alabama, USA.
Stefanescu, D. M. (2002). *Science and Engineering of Casting Solidification.* New York: Kluwer Academic, Plenum Publishers.
StJohn, D. H. (1990). *Acta Metall. Mater.* **38**, 631–636.
StJohn, D. H., Cao, P., Qian, M. & Easton, M. A. (2007). *Adv. Eng. Mater.* **9**, 739–746.
StJohn, D. H. & Qian, M. (2009). *Int. J. Cast Metal Res.* **22**, 256–259.
StJohn, D. H., Qian, M., Easton, M. A. & Cao, P. (2011). *Acta Mater.* **59**, 4907–4921.
StJohn, D. H., Qian, M., Easton, M. A., Cao, P. & Hildebrand, Z. (2005). *Metall. Mater. Trans. A*, **36**, 1669–1679.
Turnbull, D. & Vonnegut, B. (1952). *Ind. Eng. Chem.* **44**, 1292–1298.
Villars, P. (2006). ASM Alloy Phase Diagrams Database. ASM International, Materials Park, OH, USA.
Wang, F., Liu, Z. L., Qiu, D., Taylor, J. A., Easton, M. & Zhang, M. X. (2013). *Acta Mater.* **61**, 360–370.
Wang, F., Qiu, D., Liu, Z. L., Taylor, J. A., Easton, M. & Zhang, M. X. (2013). *Acta Mater.* **61**, 5636–5645.
Wang, F., Qiu, D., Liu, Z.-L., Taylor, J. A., Easton, M. A. & Zhang, M.-X. (2014). *J. Appl. Cryst.* **47**, 770–779.
Zeng, Y., Jiang, B., Zhang, M. X., Yin, H., Li, R. & Pan, F. (2014). *Intermetallics*, **45**, 18–23.
Zhang, H. H. (2008). *Trans. Nonferrous Met. Soc. China*, **18**, 836–841.
Zhang, M. X. & Kelly, P. M. (2005*a*). *Acta Mater.* **53**, 1073–1084.
Zhang, M. X. & Kelly, P. M. (2005*b*). *Acta Mater.* **53**, 1085–1096.
Zhang, M. X., Kelly, P. M., Easton, M. & Taylor, J. A. (2005). *Acta Mater.* **53**, 1427–1438.
Zhang, M. X., Kelly, P. M., Qian, M. & Taylor, J. A. (2005). *Acta Mater.* **53**, 3261–3270.